Gradient-metasurface directional photodetectors

JIANING LIU AND ROBERTO PAIELLA*

Department of Electrical and Computer Engineering and Photonics Center, Boston University, 8 Saint Mary's Street, Boston, MA 02215
**Corresponding author: rpaiella@bu.edu*

Received XX Month XXXX; revised XX Month, XXXX; accepted XX Month XXXX; posted XX Month XXXX (Doc. ID XXXXX); published XX Month XXXX

Angle-sensitive photodetectors are a promising device technology for many advanced imaging functionalities, including lensless compound-eye vision, lightfield sensing, optical spatial filtering, and phase imaging. Here we demonstrate the use of plasmonic gradient metasurfaces to tailor the angular response of generic planar photodetectors. The resulting devices rely on the phase-matched coupling of light incident at select geometrically tunable angles into guided plasmonic modes, which are then scattered and absorbed in the underlying photodetector active layer. This approach naturally introduces sharp peaks in the angular response, with smaller footprint and reduced guided-mode radiative losses (and therefore improved spatial resolution and sensitivity) compared to analogous devices based on diffractive coupling. More broadly, these results highlight a promising new application space of flat optics, where gradient metasurfaces are integrated within image sensors to enable unconventional capabilities with enhanced system miniaturization and design flexibility.

Photodetectors are ubiquitous in science, technology, and everyday life, and are traditionally designed for the sensitive detection of optical intensity, at the expense of all other degrees of freedom of the incident light (phase, polarization, wavelength, angular momentum). As a result, the measurement of these additional properties generally requires the use of bulky and complex systems, e.g., based on interferometry, polarimetry, spectral and spatial filtering. In recent years, the development of more functional light sensors capable of measuring multiple degrees of freedom simultaneously has emerged as a new topic of extensive research [1, 2], motivated by increasingly demanding applications. A particularly important functionality in this context is the ability to detect the local direction of light propagation. Combined with computational imaging techniques, this capability can enable multiple advanced imaging modalities, such as compound-eye vision with ultrawide field of view, lightfield sensing for 3D imaging, optical spatial filtering in computer vision, and the visualization of transparent phase objects by wavefront sensing.

The simplest implementation of directional image sensors involves paired combinations of suitably aligned microlenses and photodetectors [3, 4]. However, the resulting systems suffer from limited spatial resolution and field of view, due to a fundamental tradeoff between size and numerical aperture in microlenses. An alternative approach involves the integration of diffractive elements on the photodetector illumination window to selectively transmit or block incident light depending on its direction of propagation. In one implementation, stacked gratings based on the Talbot effect have been used to produce a sinusoidal dependence of responsivity on angle of incidence [5, 6]. More recently, photodetectors coated with plasmonic grating couplers have been developed featuring geometrically tunable peaks in their angular response [7-9]. Several advanced imaging functionalities have also been demonstrated in these reports, including microscale cameras and lightfield imagers [5], lensless compound-eye vision [7], optical edge detection [6, 8], and quantitative phase imaging [9]. However, the diffractive operating principle of these devices severely restricts their design flexibility, for example to decouple the angular and spectral responses for broadband achromatic operation. Wavefront sensing has also been reported based on near-field scattering by micro-apertures across adjacent pixels [10], which provides a rather weak wavelength dependence at the expense of limited ability to control the shape of the angular response.

In this work, we describe the development of angle-sensitive photodetectors based on the gradient metasurface (GMS) design platform, motivated by its distinctive ability to provide enhanced miniaturization and multifunctional operation. To date, plasmonic and dielectric GMSs have mostly been used as free-space passive components, designed to shape the incident optical wavefronts according to a desired device operation (e.g., light focusing, polarization control, holographic projection) [11, 12]. In the context of integrated devices, they have been employed for the detection of orbital angular momentum [13], directional light emission [14-16], and to interface waveguided modes to free space radiation [17-21]. For the directional photodetectors presented below, the GMSs are designed to phase-match light incident at select detection angles to surface plasmon polaritons (SPPs) on a metal film. The excited SPPs are then scattered into the underlying photodetector active layer (a

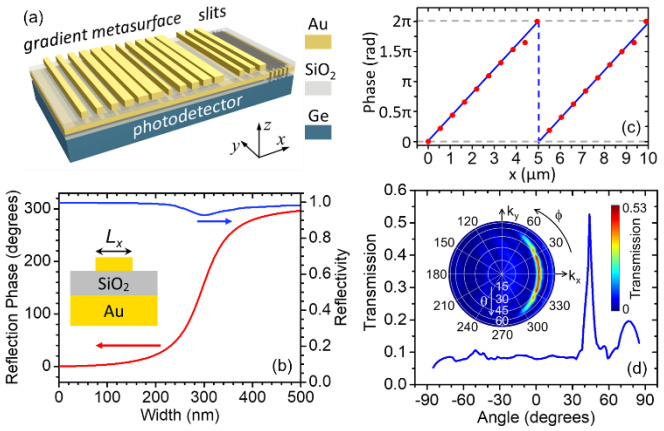

Fig. 1. GMS design. (a) Schematic device geometry. (b) Reflection phase (red trace) and amplitude squared (blue trace) of the GMS unit cell shown in the inset, computed as a function of nanostripe width L_x for normally-incident x-polarized light at $\lambda_0 = 1550$ nm. (c) Reflection phase vs nanostripe center position for a GMS designed to promote directional photodetection peaked at $\theta_p = 45°$. (d) Transmission coefficient of the GMS of (c) computed as a function of polar illumination angle θ on the x-z plane. Inset: transmission coefficient of the same device vs in-plane wavevector of the incident light.

near-infrared Ge photoconductor) by a set of subwavelength slits perforated through the metal film.

The resulting device structure is shown schematically in Fig. 1(a). The photodetector illumination window is coated with a SiO_2/Au/SiO_2 stack (60/100/60-nm-thick) supporting an aperiodic array of 50-nm-thick Au nanostripes. In this geometry, the p-polarized reflection phase of each unit cell can be tuned across a large fraction of the entire 2π phase space by varying the nanostripe width L_x, as shown by the finite difference time domain (FDTD) simulation results of Fig. 1(b) for an incident wavelength $\lambda_0 = 1550$ nm. This large phase tunability is enabled by the coupling between the nanostripe plasmonic resonances and their dipolar images in the metal film [18, 22]. At the same time, the unit-cell reflection coefficient remains quite large (> 90%) for all values of L_x [blue trace of Fig. 1(b)]. In the present devices, the nanostripe widths are selected so that their reflection phase varies linearly with their center position along the x direction, leading to a discretized version of the linear phase profile $\Phi_x = \xi x \pmod{2\pi}$ [Fig. 1(c)]. As a result, SPPs on the underlying metal film can be excited by p-polarized light with in-plane wavevector $\mathbf{k}_{\parallel}$ satisfying the phase-matching condition $\mathbf{k}_{\parallel} + \xi\hat{\mathbf{x}} = \mathbf{k}_{SPP}$. These SPPs are then intercepted by the adjacent slits where they are preferentially scattered into the Ge substrate, due to its higher refractive index (and therefore higher density of radiation modes) compared to the air above. Light incident along any other direction is instead reflected back into free space, leading to a highly directional asymmetric angular response.

Figure 1(d) shows FDTD simulation results for the transmission coefficient of a GMS designed for peak detection at a polar angle $\theta_p = 45°$, computed as a function of polar θ and azimuthal ϕ illumination angles, or equivalently as a function of $\mathbf{k}_{\parallel}$. The array contains 29 unit cells, where neighboring nanostripes have center-to-center distance $\delta x = 550$ nm and reflection phase differing by $\delta\Phi_x = 39°$. The nanostripe widths range from 0 (corresponding to a missing nanostripe in the respective unit cell) to 500 nm. The resulting phase gradient $\xi = \delta\Phi_x/\delta x$ produces the desired value of θ_p according to the phase matching condition for light propagating on the x-z plane, i.e., $2\pi\sin\theta_p/\lambda_0 + \xi = 2\pi n_{SPP}/\lambda_0$, where n_{SPP} is the SPP effective index. The design simulation results of Fig. 1(d) are fully consistent with expectations. In the angular response map shown in the inset, high transmission through the GMS is obtained only for a narrow set of values of $\mathbf{k}_{\parallel}$ determined by the SPP phase matching condition. For incident light propagating on the x-z plane [main plot of Fig. 1(d)], the transmission peak is centered near the target detection angle $\theta_p = 45°$ with a small linewidth $\delta\theta = 6.0°$ full width at half maximum (FWHM) and maximum value $T_{max} = 53\%$. For comparison, the Fresnel transmission coefficient of the Ge/air interface is about $T_{ref} = 62\%$, so that the transmission penalty introduced by the GMS is quite small ($T_{max}/T_{ref} = 85\%$). Additional simulation results (not included) show that for s-polarized light the GMS transmission is negligibly small (< 0.3%) at all angles, which is a consequence of the longitudinal nature of SPPs. This polarization dependence limits the device sensitivity for applications involving unpolarized light, although it could also be exploited to enable polarization vision for improved imaging contrast.

The nanostripe array just described essentially behaves like a plasmonic-waveguide coupler. Unlike typical applications of such devices, however, here the angular response must be controlled for all possible angles of incidence across the full hemisphere, which introduces two additional design considerations. First, the nanostripe dimensions must be selected to avoid any periodic repetition across the array. Otherwise, the GMS would simultaneously approximate discretized versions of additional linear phase profiles (modulo 2π) with slopes equal to integral multiples of ξ [14], leading to the appearance of additional peaks in the angular response. Second, it has been shown that a GMS with linear phase profile supports driven surface waves whenever no radiative channels exist for the reflected light [23]. Such surface waves are also excited in the device of Fig. 1 and can potentially produce a strong increase in the transmission background at large angles of incidence. In the present work, however, we found that, unlike SPPs, these surface waves are predominantly scattered into free space before reaching the slits, even for moderate separations (960 nm in Fig. 1) between the slit and nanostripe sections. As a result, their contribution to the GMS transmission is quite small [e.g., limited to the small bump observed near 75° in Fig. 1(d)].

The overall device architecture of Fig. 1 was designed building on our prior work of refs. 7-9, where directional photodetection was achieved through the selective excitation of SPPs by a periodic diffraction grating. Asymmetry in the angular response was then introduced by surrounding the grating coupler with slits on one side

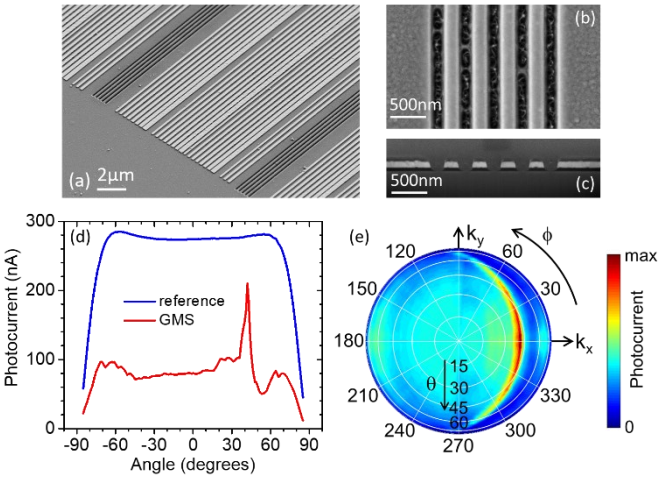

Fig. 2. Measurement results for a GMS device based on the design of Fig. 1. (a) SEM image of the GMS. (b), (c) Top-view (b) and cross-sectional (c) SEM images of a slit section. (d) Photocurrent measured with the same device (red trace) and with a nominally identical photodetector without any metasurface (blue trace) versus polar angle of incidence θ on the x-z plane of Fig. 1(a). (e) Measured photocurrent of the same GMS device as a function of both illumination angles θ and ϕ. The device bias in these measurements is 1 V. The incident light is linearly polarized on the x-z plane with 1-mW power at the laser output and approximately 14 μW on the device surface.

and a nanostripe-array "reflector" on the other, designed to scatter all incoming SPPs back into free space. Compared to these diffractive devices, the present approach has several important advantages. First, by removing the reflector section, the pixel size is reduced (without sacrificing angular sensitivity), leading to a proportional increase in spatial resolution for imaging applications. In fact, for the device of Fig. 1(d), the full lateral dimension including GMS and slits section is 20.1 μm, versus 27.2 μm for the design reported in ref. 7 featuring the same angle of peak detection $\theta_p = 45°$ and similar (actually larger) linewidth $\delta\theta = 7.6°$. Second, the present device also provides larger peak transmission [T_{max} = 53% in Fig. 1(d) versus 38% for the same baseline structure of ref. 7], and thus higher sensitivity. This improvement is mostly ascribed to the suppressed radiative scattering of SPPs in the presence of the GMS linear phase gradient compared to periodic gratings, leading to higher SPP coupling efficiency [23]. Furthermore, with the use of more complex meta-unit geometries, the GMS platform of Fig. 1 can be extended to enable capabilities that are not accessible with diffractive devices. Examples of practical interest include broadband achromatic operation, polarization independent response, and multifunctional operation such as the simultaneous measurement of angle of incidence and polarization.

The GMS of Fig. 1 was fabricated on the illumination window of a Ge metal-semiconductor-metal (MSM) photoconductor. Scanning electron microscopy (SEM) images of a resulting sample are shown in Figs. 2(a)-(c). In the device fabrication process, the SiO_2 and Au films are deposited by rf sputtering and electron-beam evaporation, respectively. The Au film is patterned by photolithography to form the GMS back reflector and the two surrounding MSM electrodes. The SiO_2 films feature suitably positioned apertures to allow for device biasing and current extraction. The GMS nanostripes are fabricated by electron-beam lithography (followed by Au electron-beam evaporation and liftoff), and focused ion beam milling is used to pattern the slits. It should also be noted that our experimental samples consist of a few (7-9) identical repetitions of the structure of Fig. 1(a), with each nanostripe-array section surrounded symmetrically by two sets of slits [see Fig. 2(a)]. This arrangement, combined with a large (300 μm) electrode separation, is convenient for the angle-resolved photocurrent measurements, because it eliminates the need for tightly focused incident light which would degrade the angular resolution. Furthermore, it allows for a more conclusive demonstration of the asymmetric angular response of the GMS, where no SPPs are excited in the "backward" direction [the negative x direction of Fig. 1(a)] which would otherwise cause crosstalk and spurious signals in a pixel array.

The experimental samples were characterized by angle-resolved photocurrent measurements with polarized laser light, using the procedure described in ref. 7. The incident wavelength was set to 1610 nm, selected to maximize the angular detection peak (similar results were measured over a small wavelength range of a few 10 nm, beyond which larger variations were observed). This optimal value is somewhat larger (~ 4%) than the design wavelength λ_0 = 1550 nm, which is attributed to small deviations of the device geometrical parameters from their target values. With this adjustment, the measurement results are in good agreement with the design simulations. A sharp peak centered at $\theta_p = 42°$ with FWHM of about 9° is observed in the plot of photocurrent versus polar angle of incidence on the plane perpendicular to the nanostripes [red trace in Fig. 2(d)]. The angular response map across the full hemisphere [Fig. 2(e)] contains a similarly narrow region of high responsivity with a characteristic curved shape that originates from the phase-matched excitation of SPPs with different wavevectors. The peak-to-average-background ratio in this plot is ~3 versus ~5 in the GMS transmission map of Fig. 1(d). This difference is mostly ascribed to the finite Au surface roughness in the experimental sample, which can scatter some of the incident light into SPPs regardless of its direction of propagation (a similar background enhancement was observed in the diffractive devices of ref. 7). Finally, the blue trace in Fig. 2(d) was measured from a reference sample without any metasurface, but otherwise based on the same geometry and featuring similar dark resistance of ~800 Ω (in these Ge MSM devices the resistance has been observed to scale with quantum efficiency, likely due to fabrication-induced surface defects affecting the carrier density [7]). At the angle of peak detection, the responsivity of the metasurface device (red trace) is as large as 75% of that of the reference sample, reasonably close to the predicted transmission ratio T_{max}/T_{ref} = 85% discussed above.

Finally, Fig. 3 shows angle-resolved photocurrent data measured with two other devices based on the architecture of Fig. 1(a), illustrating the geometrical tunability of the angle of peak detection.

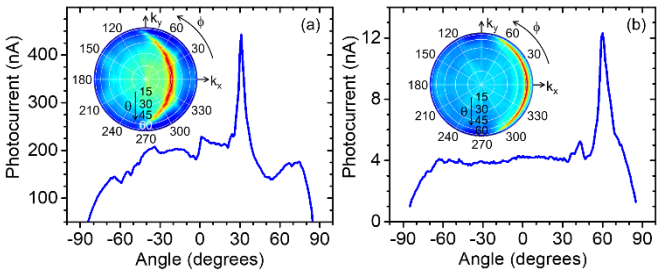

Fig. 3. Geometrical tunability of the angle of peak detection θ_p. (a) Inset: photocurrent versus polar and azimuthal illumination angles measured with a GMS device designed for peak detection at $\theta_p = 30°$. Main plot: horizontal line cut of the color map. (b) Same as (a) for a different device with $\theta_p = 60°$. The incident wavelength is 1560 nm in (a) and 1630 nm in (b). The device of panel (a) [panel (b)] produces significantly larger [smaller] photocurrent compared to the sample of Fig. 2, which correlates with its larger (smaller) dark resistance of over 1000 Ω (less than 20 Ω) [7].

Both samples contain 31 nanostripes with nearest-neighbor separation and reflection-phase difference $\delta x = 610$ nm and $\delta\Phi_x = 74°$ in Fig. 3(a), $\delta x = 590$ nm and $\delta\Phi_x = 20°$ in Fig. 3(b). A pronounced peak in the angular response is again obtained in each plot, with maximum response at $\theta_p = 30°$ in Fig. 3(a) and 60° in Fig. 3(b), in good agreement with the SPP phase matching condition discussed above. The device of Fig. 3(b) also features particularly large contrast and flat background, which may be related to its smaller phase difference $\delta\Phi_x$ between neighboring nanostripes. In this case, the desired linear phase profile is more accurately approximated by the discretized version implemented in the GMS, leading to increased robustness against fabrication imperfections. Even sharper peaks can be expected by further optimizing the fabrication process to minimize surface roughness and improve control of the nanostripe dimensions.

In summary, these results demonstrate the ability to tailor the angular response of generic planar photodetectors through the integration of plasmonic GMSs on their illumination window and offer general guidelines for the design of suitable metasurfaces. The resulting directional image sensors are promising for multiple applications within the growing field of computational imaging. In analogy with extensive prior work in free-space flat optics, we also expect that more complex GMSs within the same architecture can be developed to enable additional advanced capabilities such as achromatic response, polarization independent operation, and multifunctional behavior.

Funding. National Science Foundation (ECCS-2139451).

Acknowledgments. The FDTD simulations were performed using the Shared Computing Cluster facility at Boston University. Some of the fabrication tasks were carried out at the Center for Nanoscale Systems of Harvard University.

Disclosures. The authors declare no conflicts of interest.

Data availability. Data underlying the results presented in this paper are not publicly available at this time but may be obtained from the authors upon reasonable request.

References

1. L. Gao, Y, Qu, L. Wang, and Z. Yu, Nanophotonics 11, 2507–2529 (2022).
2. S. Yuan, C. Ma, E. Fetaya, T. Mueller, D. Naveh, F. Zhang, and F. Xia, Science 379, eade1220 (2023).
3. E. Y. Lam, J. Opt. Soc. Am. A 32, 2021–2032 (2015).
4. J. Duparré, P. Dannberg, P. Schreiber, A. Bräuer, and A. Tünnermann, Appl. Opt. 44, 2949-2956 (2005).
5. S. Jayasuriya, S. Sivaramakrishnan, E. Chuang, D. Guruaribam, A. Wang, and A. Molnar, Opt. Lett. 40, 2433-2436 (2015).
6. H. G. Chen, S. Jayasuriya, J. Yang, J. Stephen, S. Sivaramakrishnan, A. Veeraraghavan, and A. Molnar, Proceedings of the IEEE Conference on Computer Vision and Pattern Recognition, 903–912 (2016).
7. L. C. Kogos, Y. Li, J. Liu, Y. Li, L. Tian, and R. Paiella, Nat. Commun. 11, 1637 (2020).
8. J. Liu, H. Wang, L. C. Kogos, Y. Li, Y. Li, L. Tian, and R. Paiella, Opt. Express 30, 29074–29087 (2022).
9. J. Liu, H. Wang, Y. Li, L. Tian, and R. Paiella, Nanophotonics 12, 3519-3528 (2023).
10. S. Yi, J. Xiang, M. Zhou, Z. Wu, L. Yang, and Z. Yu, Nat. Commun. 12, 6002 (2021).
11. P. Genevet, F. Capasso, F. Aieta, M. Khorasaninejad, and R. Devlin, Optica 4, 139-152 (2017).
12. F. Ding, A. Pors, and S. I. Bozhevolnyi, Rep. Prog. Phys. 81, 026401 (2018).
13. P. Genevet, J. Lin, M. A. Kats, and F. Capasso, Nat. Commun. 3, 1278 (2012).
14. X. Wang, Y. Li, R. Toufanian, L. C. Kogos, A. Dennis, and R. Paiella, Adv. Opt. Mater. 8, 1901951 (2020).
15. P. P. Iyer, R. A. DeCrescent, Y. Mohtashami, G. Lheureux, N. A. Butakov, A. Alhassan, C. Weisbuch, S. Nakamura, S. P. DenBaars, and J. A. Schuller, Nat. Photon. 14, 543-549 (2020).
16. Y.-Y. Xie, P.-N. Ni, Q.-H. Wang, Q. Kan, G. Briere, P.-P. Chen, Z.-Z. Zhao, A. Delga, H.-R. Ren, H.-D. Chen, C. Xu, and P. Genevet, Nat. Nanotechnol. 15, 125–130 (2020).
17. H. Lingling, C. Xianzhong, B. Benfeng, T. Qiaofeng, J. Guofan, T. Zentgraf, S. Zhang, Light: Sci. Appl. 2, e70 (2013).
18. A. Pors, M. G. Nielsen, T. Bernardin, J.-C. Weeber, and S. I. Bozhevolnyi, Light: Sci. Appl. 3, e197 (2014).
19. Y. Meng, Y. Chen, L. Lu, Y. Ding, A. Cusano, J. A. Fan, Q. Hu, K. Wang, Z. Xie, Z. Liu, Y. Yang, Q. Liu, M. Gong, Q. Xiao, S. Sun, M. Zhang, X. Yuan, and X. Ni, Light: Sci. Appl. 10, 235 (2021).
20. H. Huang, A. C. Overvig, Y. Xu, S. C. Malek, C.-C. Tsai, A. Alù, and N. Yu, Nat. Nanotechnol. 18, 580–588 (2023).
21. Y. Chen, X. Zheng, X. Zhang, W. Pan, Z. Wang, S. Li, S. Dong, F. Liu, Q. He, L. Zhou, and S. Sun, Nano Lett. 23, 3326–3333 (2023).
22. S. Sun, K.-Y. Yang, C.-M. Wang, T.-K. Juan, W. T. Chen, C. Y. Liao, Q. He, S. Xiao, W.-T. Kung, G.-Y. Guo, L. Zhou, and D. P. Tsai, Nano Lett. 12, 6223-6229 (2012).
23. S. Sun, Q. He, S. Xiao, Q. Xu, X. Li, and L. Zhou, Nat. Mater. 11, 426-431 (2012).

References

1. L. Gao, Y, Qu, L. Wang, and Z. Yu, "Computational spectrometers enabled by nanophotonics and deep learning," Nanophotonics 11, 2507–2529 (2022).
2. S. Yuan, C. Ma, E. Fetaya, T. Mueller, D. Naveh, F. Zhang, and F. Xia, "Geometric deep optical sensing," Science 379, eade1220 (2023).
3. E. Y. Lam, "Computational photography with plenoptic camera and light field capture: tutorial," J. Opt. Soc. Am. A 32, 2021–2032 (2015).
4. J. Duparré, P. Dannberg, P. Schreiber, A. Bräuer, and A. Tünnermann, "Thin compound-eye camera," Appl. Opt. 44, 2949-2956 (2005).
5. S. Jayasuriya, S. Sivaramakrishnan, E. Chuang, D. Guruaribam, A. Wang, and A. Molnar, "Dual light field and polarization imaging using CMOS diffractive image sensors," Opt. Lett. 40, 2433-2436 (2015).
6. H. G. Chen, S. Jayasuriya, J. Yang, J. Stephen, S. Sivaramakrishnan, A. Veeraraghavan, and A. Molnar, "ASP vision: Optically computing the first layer of convolutional neural networks using angle sensitive pixels," Proceedings of the IEEE Conference on Computer Vision and Pattern Recognition, 903–912 (2016).
7. L. C. Kogos, Y. Li, J. Liu, Y. Li, L. Tian, and R. Paiella, "Plasmonic ommatidia for lensless compound-eye vision," Nat. Commun. 11, 1637 (2020).
8. J. Liu, H. Wang, L. C. Kogos, Y. Li, Y. Li, L. Tian, and R. Paiella, "Optical spatial filtering with plasmonic directional image sensors," Opt. Express 30, 29074–29087 (2022).
9. J. Liu, H. Wang, Y. Li, L. Tian, and R. Paiella, "Asymmetric metasurface photodetectors for single-shot quantitative phase imaging," Nanophotonics 12, 3519-3528 (2023).
10. S. Yi, J. Xiang, M. Zhou, Z. Wu, L. Yang, and Z. Yu, "Angle-based wavefront sensing enabled by the near fields of flat optics," Nat. Commun. 12, 6002 (2021).
11. P. Genevet, F. Capasso, F. Aieta, M. Khorasaninejad, and R. Devlin, "Recent advances in planar optics: from plasmonic to dielectric metasurfaces," Optica 4, 139-152 (2017).
12. F. Ding, A. Pors, and S. I. Bozhevolnyi, "Gradient metasurfaces: a review of fundamentals and applications," Rep. Prog. Phys. 81, 026401 (2018).
13. P. Genevet, J. Lin, M. A. Kats, and F. Capasso, "Holographic detection of the orbital angular momentum of light with plasmonic photodiodes," Nat. Commun. 3, 1278 (2012).
14. X. Wang, Y. Li, R. Toufanian, L. C. Kogos, A. Dennis, and R. Paiella, "Geometrically-tunable beamed light emission from a quantum-dot ensemble near a gradient metasurface," Adv. Opt. Mater. 8, 1901951 (2020).
15. P. P. Iyer, R. A. DeCrescent, Y. Mohtashami, G. Lheureux, N. A. Butakov, A. Alhassan, C. Weisbuch, S. Nakamura, S. P. DenBaars, and J. A. Schuller, "Unidirectional luminescence from InGaN/GaN quantum-well metasurfaces," Nat. Photon. 14, 543-549 (2020).
16. Y.-Y. Xie, P.-N. Ni, Q.-H. Wang, Q. Kan, G. Briere, P.-P. Chen, Z.-Z. Zhao, A. Delga, H.-R. Ren, H.-D. Chen, C. Xu, and P. Genevet, "Metasurface-integrated vertical cavity surface-emitting lasers for programmable directional lasing emissions," Nat. Nanotechnol. 15, 125–130 (2020).
17. H. Lingling, C. Xianzhong, B. Benfeng, T. Qiaofeng, J. Guofan, T. Zentgraf, S. Zhang, "Helicity dependent directional surface plasmon polariton excitation using a metasurface with interfacial phase discontinuity," Light Sci. Appl. 2, e70 (2013).
18. A. Pors, M. G. Nielsen, T. Bernardin, J.-C. Weeber, and S. I. Bozhevolnyi, "Efficient unidirectional polarization-controlled excitation of surface plasmon polaritons," Light: Sci. Appl. 3, e197 (2014).
19. Y. Meng, Y. Chen, L. Lu, Y. Ding, A. Cusano, J. A. Fan, Q. Hu, K. Wang, Z. Xie, Z. Liu, Y. Yang, Q. Liu, M. Gong, Q. Xiao, S. Sun, M. Zhang, X. Yuan, and X. Ni, "Optical meta-waveguides for integrated photonics and beyond," Light Sci. Appl. 10, 235 (2021).
20. H. Huang, A. C. Overvig, Y. Xu, S. C. Malek, C.-C. Tsai, A. Alù, and N. Yu, "Leaky-wave metasurfaces for integrated photonics," Nat. Nanotechnol. 18, 580–588 (2023).
21. Y. Chen, X. Zheng, X. Zhang, W. Pan, Z. Wang, S. Li, S. Dong, F. Liu, Q. He, L. Zhou, and S. Sun, "Efficient meta-couplers squeezing propagating light into on-chip subwavelength devices in a controllable way," Nano Lett. 23, 3326–3333 (2023).
22. S. Sun, K.-Y. Yang, C.-M. Wang, T.-K. Juan, W. T. Chen, C. Y. Liao, Q. He, S. Xiao, W.-T. Kung, G.-Y. Guo, L. Zhou, and D. P. Tsai, "High-efficiency broadband anomalous reflection by gradient meta-surfaces," Nano Lett. 12, 6223-6229 (2012).
23. S. Sun, Q. He, S. Xiao, Q. Xu, X. Li, and L. Zhou, "Gradient-index meta-surfaces as a bridge linking propagating waves and surface waves," Nat. Mater. 11, 426-431 (2012).